Supporting Information: Temperature-controlled dripping-onto-substrate (DoS) extensional rheometry of polymer micelle solutions

Diana Y. Zhang and Michelle A. Calabrese[†]

Department of Chemical Engineering & Materials Science

University of Minnesota, Twin Cities

Minneapolis, MN, USA 55455

[†]Email: mcalab@umn.edu

Contents

SI.1   TC-DoS temperature validation and determination

To demonstrate the need for chamber insulation and an enclosure heater, test measurements on an aqueous poly(N-isopropylacrylamide) (PNIPAM) solution are shown in Figure S1. Depending on polymer concentration and molecular weight, PNIPAM solutions exhibit a transition between an optically clear and turbid state at a certain temperature, enabling the transition to be visualized with the naked eye. In our test case, the solution transitions from clear to turbid at ~34 °C, as measured by cloud point tests (Figure S1a). Without the reflective foam insulation and the enclosure heater (Figure S1b), the pendant drop formed during the measurement is still optically clear when the nozzle and substrate heaters are set to 36 °C, despite the heater temperatures being 2 °C higher than the measured cloud point temperature (Figure S1b). This indicates that the actual droplet temperature is lower than the set temperature of the heaters by as much as 2 °C. After raising the nozzle and substrate heater temperatures to 37 °C, the droplet underwent the clear-turbid transition, indicating the actual droplet temperature surpassed the transition temperature of 34 °C. The discrepancy between the actual droplet temperature and the heater temperatures, as indicated by the 'lag' in the clear-turbid transition, demonstrates the need to heat the surrounding air. Thus, in the final chamber configuration used for measurements in the main text, the chamber walls were encased in reflective foam insulation, and an enclosure heater was used to increase the temperature of air inside the chamber.
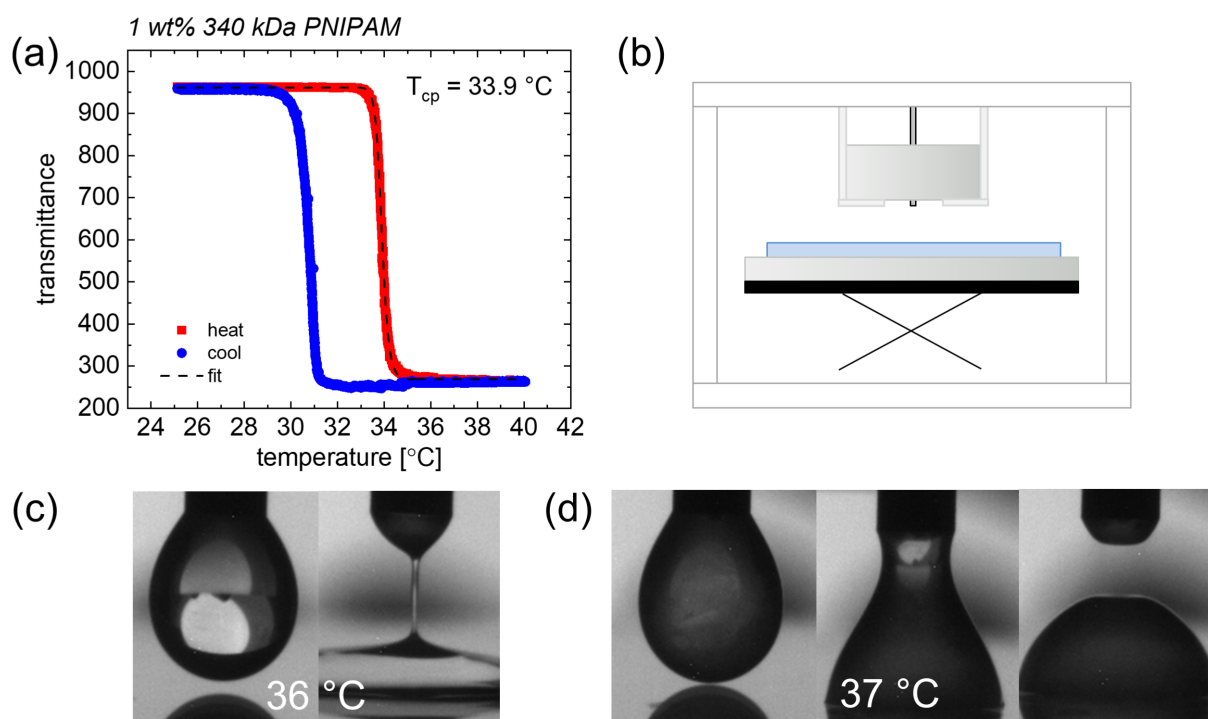
Figure S1: Justification for enclosure heater and reflective chamber insulation in TC-DoS instrumentation. (a) cloud point test shows that a 1% wt 340 kDa PNIPAM solution transitions from optically clear to turbid at ∼34 °C. (b) Chamber configuration used for measurements in this figure (no enclosure heater or insulation). (c) Droplet is still optically transparent when nozzle and substrate heaters are set to 36 °C, indicating the droplet temperature is lower than desired. (d) Droplet transitioned at a set temperature of 37 °C.

Validation of temperature control in the complete chamber configuration (with nozzle heater, substrate heater, enclosure heater, and insulation) is shown in Figure S2. Measured values are tabulated in Table S1; substrate, nozzle, and gap temperatures are within range of each other considering the temperature element (e.g. RTD) accuracies of $\pm$ 0.5 °C.

Sample needle, substrate, and chamber temperatures for trials at 35 °C are shown in Table S2. Given that average substrate and nozzle temperatures were typically within $\leq$ 0.5 °C of each other during experiments at each temperature, the average nozzle temperature was chosen as the reported temperature in the main text.

Table S1: Temperature control validation

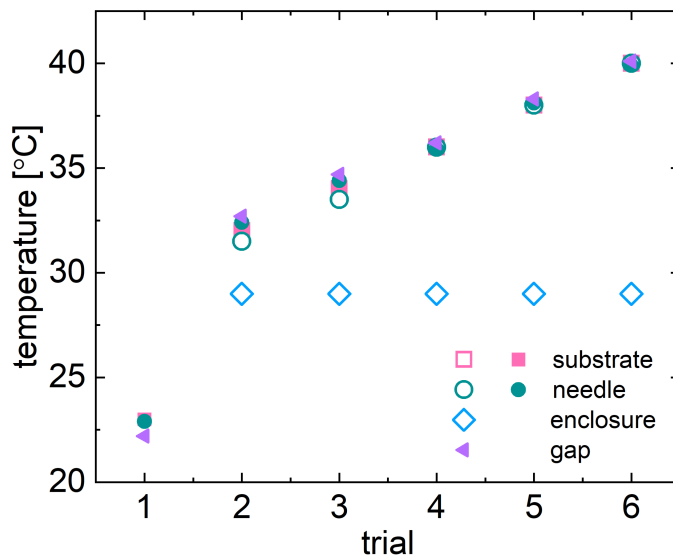| Trial	substrate		nozzle		chamber	
	T_{sp} [°C]	$T_{substrate}$ [°C]	T_{sp} [°C]	T_{nozzle} [°C]	$T_{sp,chamber}$ [°C]	T_{gap} [°C]
1	23	23.0	23	22.9	23	22.2
2	32	32.1	31.5	32.4	29	32.7
3	34	34.2	33.5	34.4	29	34.7
4	36	36.0	36	35.9	29	36.2
5	38	38.0	38	38.1	29	38.3
6	40	40.0	40	39.9	29	40.1

Figure S2: Setpoint temperatures (open symbols) and measured temperatures (closed symbols) of heaters and gap between needle and substrate during temperature control validation.

SI.2   Raw DoS data and reproducibility

Figures S3 and S4 show the entirety of low-elasticity DoS trials used for analysis, and Figures S5 and S6 show all WLM trials. Note that the radius decay features just prior to break up – below $R/R_0 \approx 0.03 - 0.04$ for 37 °C and $R/R_0 \approx 0.02 - 0.03$ for 39 °C – are not as reliable due to thresholding artifacts inherent to image processing; see SI.2.2 for details. Thus, the 39 °C data are truncated accordingly. At least five DoS trials ($N \geq 5$) were used for analyses at each condition. Statistics were calculated for parameters such as t_b and n by taking an average and reporting the 95% confidence intervals. In general, the spread in trials increases with increasing temperature and thus fluid elasticity. Comparatively, spread (and thus uncertainty) is highest in the WLM trials. Both 37 °C and 39 °C are in the transitional region in which micelle structure changes drastically with temperature. Thus, very small fluctuations in the temperature across trials

Table S2: Substrate, nozzle, and chamber temperatures for measurements at 35 °C.

Trial	T_{nozzle} [°C]	$T_{substrate}$ [°C]	$T_{chamber}$ [°C]
1	35.1	34.8	30.7
2	34.7	34.7	30.6
3	35.0	34.7	30.7
4	34.5	34.7	31.0
5	34.8	34.6	30.8
6	34.8	34.7	30.9
7	34.8	34.2	27.9
8	34.8	34.4	28.1
9	35.1	34.7	28.6

likely cause nontrivial variations in measurements. Despite the relatively larger 95 % confidence intervals in 37 °C and 39 °C trials, the average λ_E and t_b values are still statistically different at each temperature, reflecting distinct dynamics.
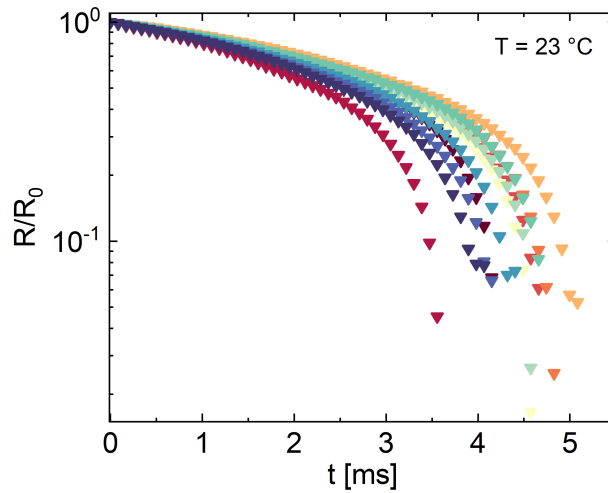
Figure S3: All D_2O DoS curves used for analysis at 23 °C ($N = 11$).
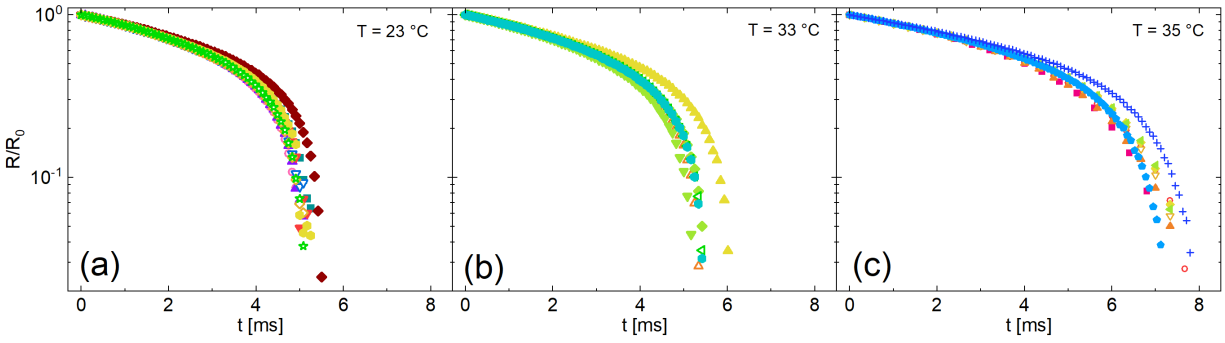
Figure S4: P234 DoS curves used for analysis at (a) 23 °C ($N = 9$), (b) 33 °C ($N = 6$), and (c) 35 °C ($N = 8$).
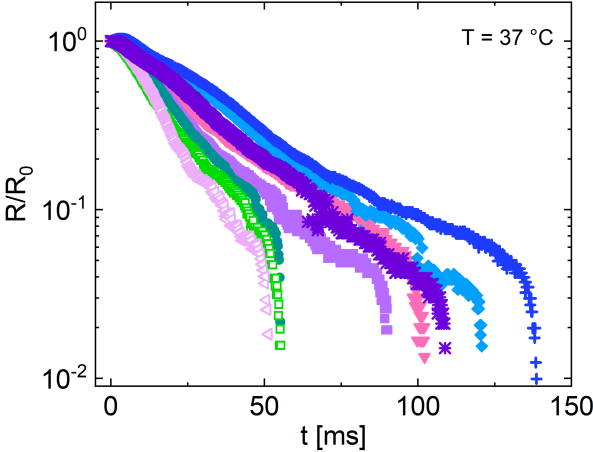
Figure S5: Radius evolution curves used for analysis for P234 at 37 °C ($N = 8$).
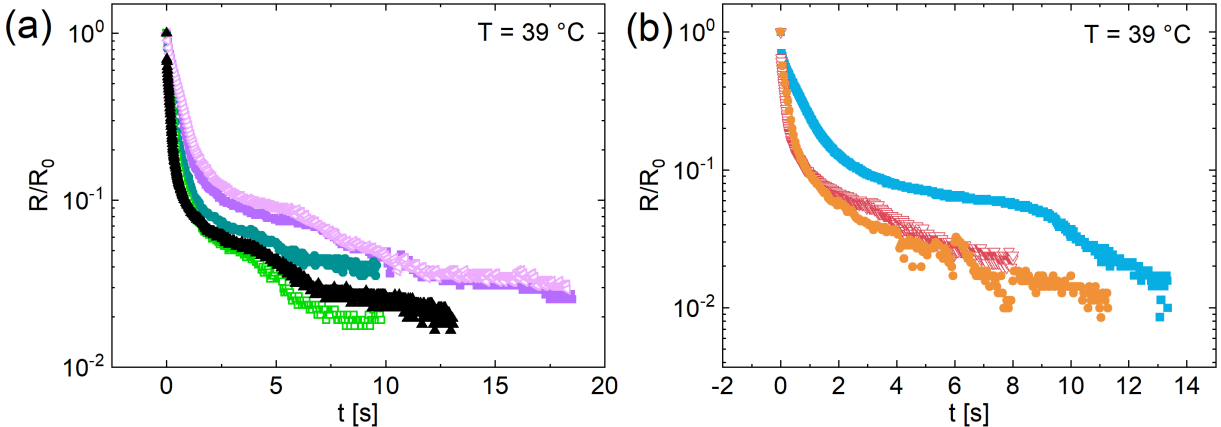
Figure S6: Raw radius evolution curves for P234 at 39 °C. (a) Trials used in analyses ($N = 5$). (b) Partial trials taken on a different day than data in (a), showing reproducibility of curve features associated with BOAS formation.

SI.2.1 Impact of temperature gradients on rheological parameters

For the trials shown in the main text, temperature gradients did not have a substantial impact on the extracted rheological parameters (t_b, λ_E, η_E^∞, t_E). Here, the temperature gradient was quantified as the difference between the substrate and nozzle heaters ($T_{diff} = T_{sub} - T_{nozzle}$) and the absolute value of that difference ($T_{diff,abs}$). Multivariate analysis comparing the substrate and needle temperatures, average temperature, T_{diff}, and $T_{diff,abs}$ and the rheological parameters showed no statistically significant trend on any of the four rheological parameters on the temperature parameters. Even in the cases where the highest correlation parameter of ~ 0.6 was obtained, the resulting $R^2 \sim 0.3$, suggesting that these variables are not well-correlated.

Multivariate — T=33 C

Correlations — The correlations are estimated by Row-wise method.

	Tsub	Tneedle	Tavg	T_diffabs	Tdiff	tb
Tsub	1.0000	0.0605	0.9965	0.2135	-0.9964	-0.3303
Tneedle	0.0605	1.0000	0.1440	0.5040	0.0242	0.3485
Tavg	0.9965	0.1440	1.0000	0.2540	-0.9858	-0.2982
T_diffabs	0.2135	0.5040	0.2540	1.0000	-0.1711	0.3163
Tdiff	-0.9964	0.0242	-0.9858	-0.1711	1.0000	0.3604
tb	-0.3303	0.3485	-0.2982	0.3163	0.3604	1.0000

Multivariate — T=35 C

Correlations — The correlations are estimated by Row-wise method.

	Tsub	Tneedle	Tavg	T_diffabs	Tdiff	lambda	tb	eta_inf	t_E
Tsub	1.0000	0.3173	0.9274	0.6257	-0.8754	-0.0974	-0.1653	-0.5813	0.3213
Tneedle	0.3173	1.0000	0.6489	-0.2627	0.1807	0.4946	0.3274	0.0476	0.1616
Tavg	0.9274	0.6489	1.0000	0.3984	-0.6311	0.1169	-0.0035	-0.4476	0.3215
T_diffabs	0.6257	-0.2627	0.3984	1.0000	-0.7829	-0.0503	-0.3155	-0.5741	0.2245
Tdiff	-0.8754	0.1807	-0.6311	-0.7829	1.0000	0.3532	0.3383	0.6271	-0.2508
lambda	-0.0974	0.4946	0.1169	-0.0503	0.3532	1.0000	0.2825	0.4663	-0.5213
tb	-0.1653	0.3274	-0.0035	-0.3155	0.3383	0.2825	1.0000	0.2528	0.2194
eta_inf	-0.5813	0.0476	-0.4476	-0.5741	0.6271	0.4663	0.2528	1.0000	-0.7236
t_E	0.3213	0.1616	0.3215	0.2245	-0.2508	-0.5213	0.2194	-0.7236	1.0000

Multivariate — T=37 C

Correlations — The correlations are estimated by Row-wise method.

	Tsub	Tneedle	Tavg	T_diffabs	Tdiff	lambda_E	tb
Tsub	1.0000	-0.0650	0.7735	0.6523	-0.8037	0.6076	0.6088
Tneedle	-0.0650	1.0000	0.5822	0.2335	0.6460	-0.0784	-0.0427
Tavg	0.7735	0.5822	1.0000	0.6798	-0.2446	0.4453	0.4689
T_diffabs	0.6523	0.2335	0.6798	1.0000	-0.3598	0.5496	0.5285
Tdiff	-0.8037	0.6460	-0.2446	-0.3598	1.0000	-0.5116	-0.4912
lambda_E	0.6076	-0.0784	0.4453	0.5496	-0.5116	1.0000	0.8731
tb	0.6088	-0.0427	0.4689	0.5285	-0.4912	0.8731	1.0000

Multivariate — T=39 C

Correlations — The correlations are estimated by Row-wise method.

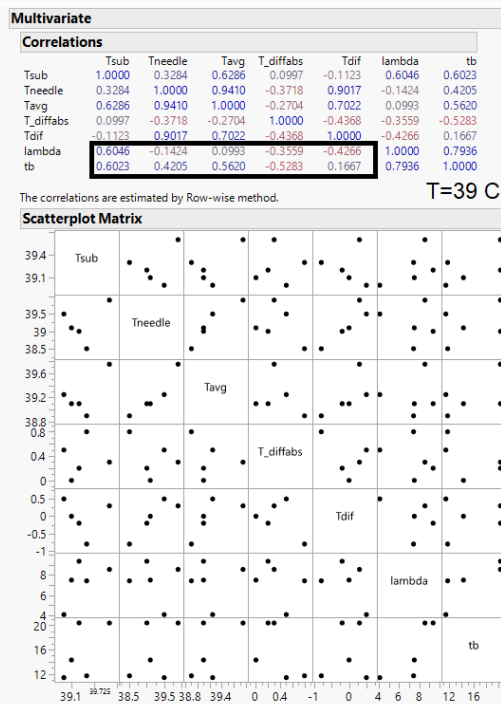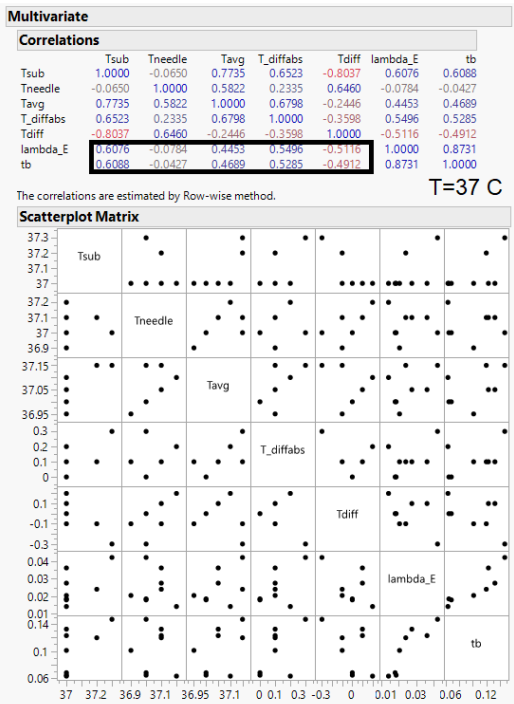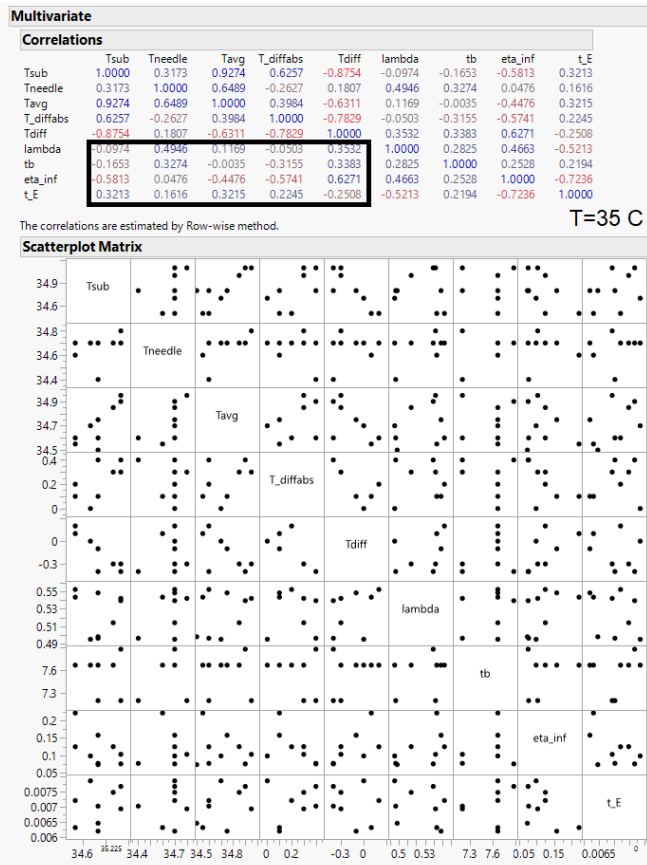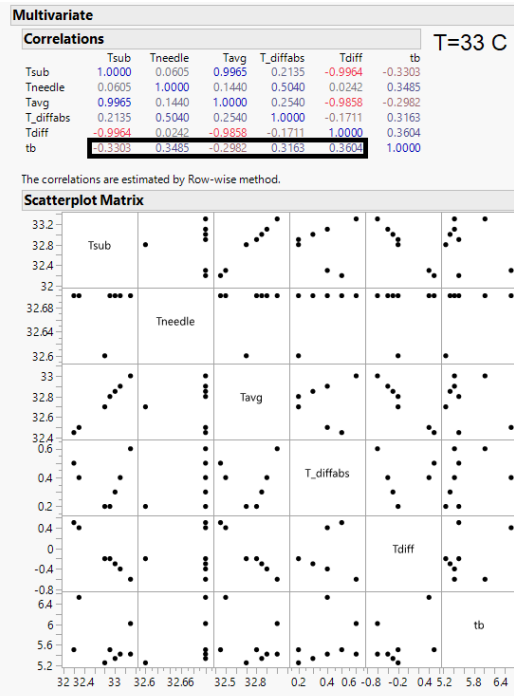|	Tsub	Tneedle	Tavg	T_diffabs	Tdif	lambda	tb
Tsub	1.0000	0.3284	0.6286	0.0997	-0.1123	0.6046	0.6023
Tneedle	0.3284	1.0000	0.9410	-0.3718	0.9017	-0.1424	0.4205
Tavg	0.6286	0.9410	1.0000	-0.2704	0.7022	0.0993	0.5620
T_diffabs	0.0997	-0.3718	-0.2704	1.0000	-0.4368	-0.3559	-0.5283
Tdif	-0.1123	0.9017	0.7022	-0.4368	1.0000	-0.4266	0.1667
lambda	0.6046	-0.1424	0.0993	-0.3559	-0.4266	1.0000	0.7936
tb	0.6023	0.4205	0.5620	-0.5283	0.1667	0.7936	1.0000

Figure S7: Multivariate analysis of temperature and gradient parameters (T_{sub}, T_{nozzle}, T_{avg}, T_{diff}, $T_{diff,abs}$ vs. DoS parameters (t_b, λ_E, η_E^{∞}, t_e) for $T = 33, 35, 37$ and $39\ °C$. At each setpoint, no significant correlations are observed between DoS parameters and temperature parameters.

SI.2.2 Terminal visco-elastocapillary (TVEC) thinning analysis

Note that the radial decay prior to breakup in raw DoS thinning profiles for trials that exhibit EC thinning (Figures S5 and S6) are affected by the thresholding step used to binarize images during image processing. In the thresholding step, a single threshold value is chosen across all images in a single stack. Thus, the final few frames in which the filament is exceptionally slender may not be captured. This issue is exacerbated by the presence of a chamber that adds an additional window that must be imaged through. The early frames should not be overthresholded to compensate because doing so would artificially increase the size of the filament. As a trade-off, the downturn at the end of the radius decay plot arises and appears to resemble terminal visco-elastocapillary (TVEC) thinning, which has been observed in high molecular weight PEO solutions.[1] The TVEC region arises from the finite extensibility of the polymer chain or micelle and can be described by the following equation: [1–3]

$$R/R_0 = \frac{\sigma}{2R_0\eta_E^\infty}(t_f - t) = \frac{1/2}{OhTr^\infty}\left(\frac{t_f - t}{t_R}\right) \tag{SI.2.1}$$

where $Tr^\infty = \eta_E^\infty/\eta_0$ is the terminal Trouton ratio.

To assess if TVEC thinning is really present, the final frames of representative P234 trials at 37 °C and 39 °C were re-thresholded independently from the earlier frames to capture more of the slender filament. For P234 at 37 °C (Figure S8a-b), the tail in the thinning profile still exists after rethresholding. Fitting Eq. SI.2.1 to the end of thinning yields an infinite extensional viscosity η_E^∞ = 14.7 Pa·s, which is slightly higher than, but within 20% of, the value estimated from calculating η_E from the radius decay data (η_E^∞ = 11.9 Pa·s). Importantly, re-thresholding does not impact the extracted λ_E, and the η_E^∞ value is still the same order of magnitude as that reported in the main text. For P234 at 39 °C, re-thresholding the final frames eliminates the downturn completely; thus, no TVEC thinning is present, and the downturn can be entirely attributed to threshold decay as the filament becomes exceedingly slender. As such, the re-thresholded frames near breakup have been added to the radius decay plot shown in the main text for P234 WLMs at 39 °C.
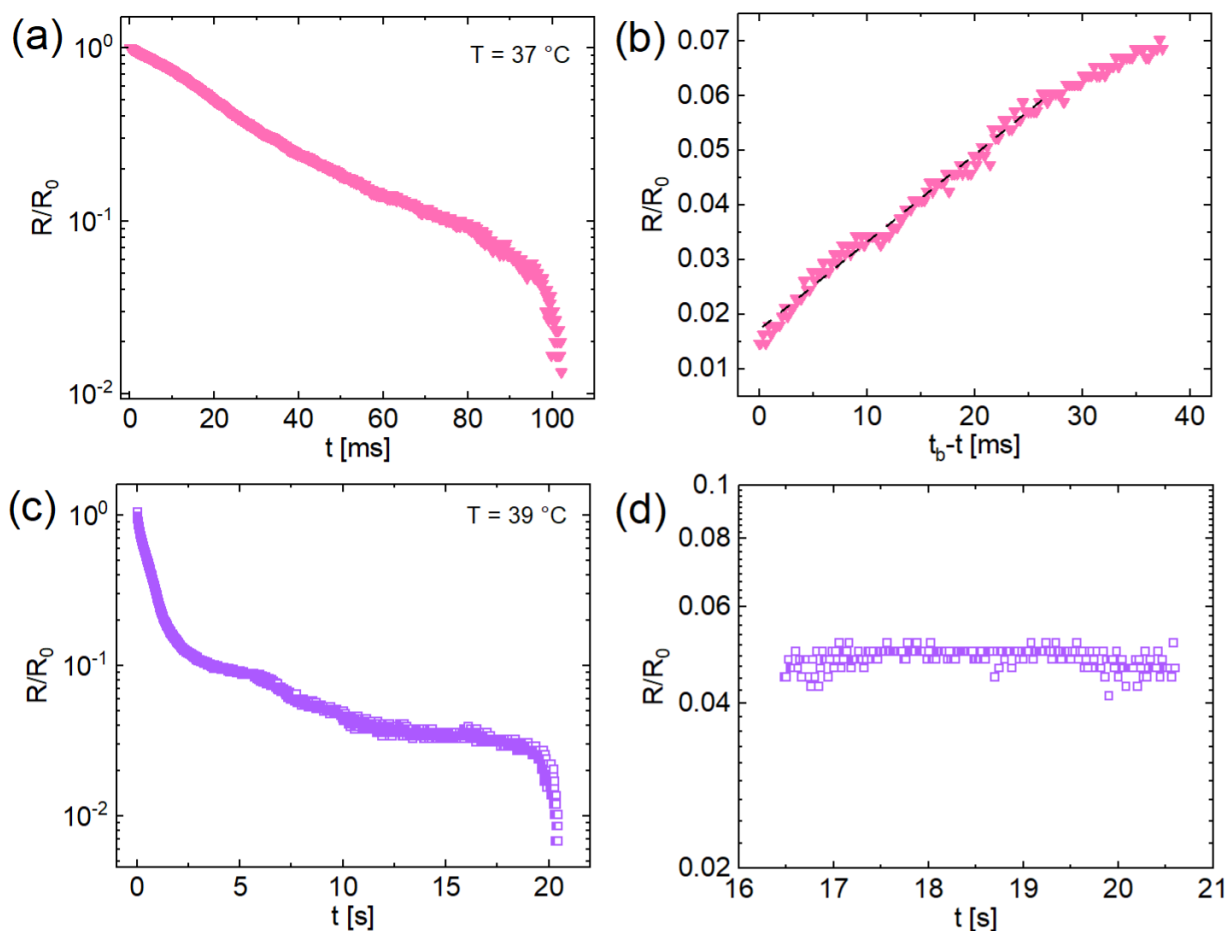
Figure S8: Original radial decay curves and re-thresholded end regions of representative P234 DoS trials. (a) original radial decay curve for P234 37 °C. (b) linearized end region resulting from re-thresholding final frames for P234 37 °C. (c) original radial decay curve for P234 39 °C. (d) curve resulting from re-thresholded final frames for P234 39 °C.

SI.3   DoS extension rates for P234 at 39 °C

The extension rates of P234 WLMs at 39 °C are significantly lower than those of high molecular weight polymers. As shown in Figure S9, the extension rates only reach $\sim$ 10 1/s at most, which is 2-3 orders of magnitude lower than those reached in high molecular weight PEO solutions.[4] The gray shaded region in Figure S9 indicates early thinning times in which spreading and VC thinning is occurring; thus, only extension rates in the nonshaded region are attributed to elastic thinning.
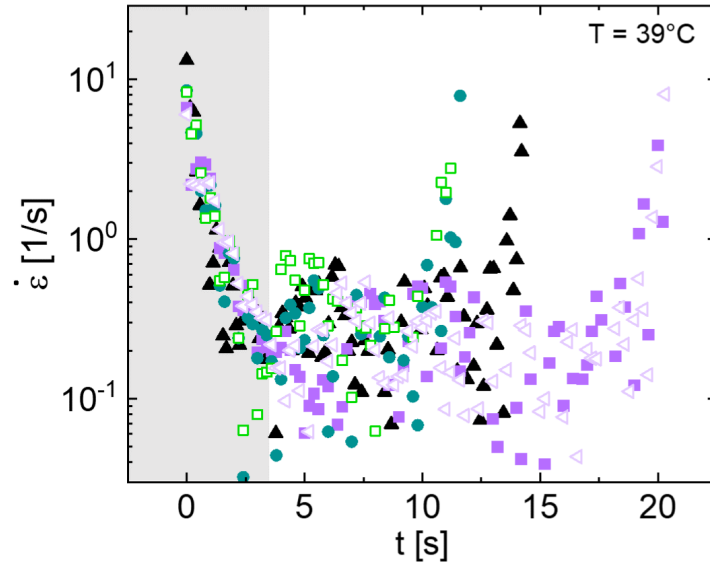
Figure S9: Extension rates of P234 at 39 °C. Curves correspond to the same trials shown in Figure S6a. The gray shaded region corresponds to early thinning times in which spreading and VC thinning occurs.

SI.4   Calculating IC prefactor and Rayleigh time

The IC prefactor α has been shown to vary between 0.4 and 1, depending on fluid and system parameters.[5] The variation of α in this work is shown in Table S3. As shown previously,[6] when α is allowed to vary such that C_{fit} and C_{calc} match, $\alpha \approx 0.6$ for fluids that exhibit IC thinning. In this work, D_2O and P234 at 23 °C exhibit IC thinning. α then deviates from 0.6 for more viscous fluids such as P234 at 33 °C and 35 °C.

Just like C_{fit} and C_{calc} in the main text, $t_{R,fit}$ and $t_{R,calc}$ are in good agreement for samples that exhibit IC thinning but deviate from each other as the samples become more viscous and elastic. This same trend was shown by Lauser *et al.*[6]. $t_{R,fit}$ and $t_{R,calc}$ differ by $\leq 10\%$ for D_2O and P234 at 23 °C, both of which exhibit IC thinning, whereas $t_{R,fit}$ and $t_{R,calc}$ for the viscoelastic samples differ by $> 40\%$.

Table S3: α values needed to match C_{fit} and C_{calc} using fluid parameters as well as t_R determined from the fit ($t_{R,fit}$) and calculated from fluid parameters ($t_{R,calc}$).

Sample	T [°C]	C_{fit}, C_{calc}	α	$t_{R,calc}$ [ms]	$t_{R,fit}$ [ms]
D_2O	23	35.1	0.56	2.0	2.2
P234	23	30.1	0.63	3.0	2.8
P234*	33	37.3	0.79	3.1	2.0
P234*	35	62.6	1.32	3.1	0.94
P234*	37	-	-	3.1	-
P234*	39	-	-	3.1	-

*samples that deviate from IC thinning

SI.5   Viscocapillary thinning at 37 °C and 39 °C

Fits to the initial thinning regime of P234 solutions at 37 °C and 39 °C yielded viscocapillary (VC) thinning behavior as expected ($Oh \gg 1$) at these temperatures. In Figure S10, thinning profiles were fit to a a power law model $R/R_0 \sim t^n$ to allow the power law exponent n to vary. Fits yielded $n = 1$ for P234 both at 37 °and 39 °C, aligning with VC model scaling (Table S4). Data and fits are presented both in the semi-log and linearized log-log format in Figure S10.

Table S4: Power law exponents from fits to initial thinning regimes in P234 at 37 °C and 39 °C reflect VC behavior. Values are reported as an average and 95 % confidence interval.

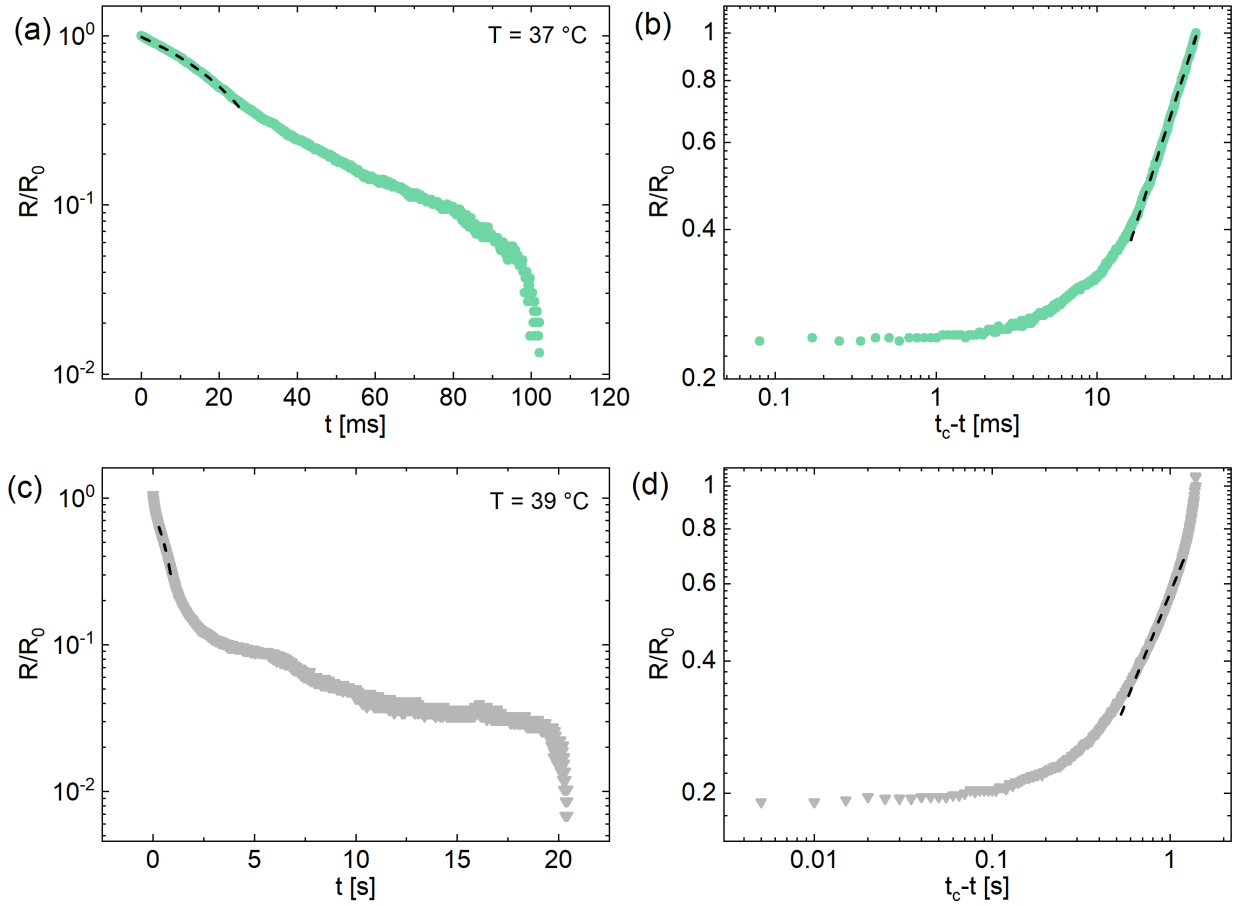|	T [°C]	n
P234	37	1.04 ± 0.03
P234	39	1.05 ± 0.05

Figure S10: Representative fits to P234 thinning data at (a-b) 37 °C and (c-d) 39 °C reflecting VC thinning behavior (n=1). Fits overlaid on linearized radius data shown in (b) and (d).

SI.6 Additional dimensionless numbers

The Bond number Bo helps determine the relative importance of gravitational effects compared to surface tension effects:

$$Bo = \frac{\Delta \rho g R_0^2}{\sigma} \tag{SI.6.1}$$

$\Delta \rho$ is the difference between the fluid and surrounding air densities, g is the gravitational constant, R_0 is the initial filament radius, and σ is the surface tension of the fluid. Generally, $Bo < 1$ suggests that surface tension forces dominate while $Bo > 1$ suggests that gravitational effects are important. However, Clasen has observed that for capillary-thinning experiments, gravitational effects can be neglected for fluids with $Bo < 0.2$.[7] By fixing Bo at 0.2, a critical liquid bridge radius R^* below which gravitational effects can be neglected can be calculated. Table S5 tabulates the calculated

Bo for D_2O and P234 at each temperature as well as the critical radius R^*. Bo for each sample is less than 1, and R^* is larger than $R_0 = 0.64$ mm for all samples. Thus, gravitational effects can be neglected for our samples.

The elastocapillary number Ec compares the viscous timescale $\eta_0 R_0/\sigma$ with the elastocapillary timescale (extensional relaxation time) λ_E:[8]

$$Ec = \frac{\lambda_E \sigma}{\eta_0 R_0} \tag{SI.6.2}$$

For $Ec \gg 1$, thinning is controlled by elasticity and thus the extensional relaxation time. For $Ec \ll 1$, thinning is controlled by viscous effects determined by η_0/σ.[7] As shown in Table S5, $Ec > 1$ for both elastic P234 samples at 37 °C and 39 °C, supporting the use of EC analysis in the main text. For P234 at 35 °C, $Ec = 0.66$ which is less than 1, suggesting viscous forces are still important. However, as shown in the main text, the radius evolution clearly deviates from power law thinning behavior, thus exhibiting weakly elastic behavior.

Clasen[7] showed that the critical local elastocapillary number Ec^*, which uses the actual filament $R(t)$ radius rather than the initial radius, is $Ec^* = 4.7015$ at the VC-EC transition. As such, the VC-EC transition is predicted to occur at a filament radius $R_{VC-EC} = 0.2127\lambda_E\sigma/\eta_0$. Using this equation, R_{VC-EC}/R_0 was calculated for P234 at 37 °C and 39 °C, as shown in Table S5. From these estimates, $R_{VC-EC}/R_0 \approx 0.1$ for P234 at 37 °C; thus, all EC fits for P234 at 37 °C were started near $R/R_0 = 0.1$.

Table S5: Calculated dimensionless numbers and critical radii for each sample studied.

Sample	T [°C]	Bo	R^*	Ec	R_{VC-EC}
D_2O	23	0.060	1.2	-	-
P234	23	0.14	0.75	-	-
P234	33	0.15	0.74	-	-
P234	35	0.15	0.74	0.66	-
P234	37	0.14	0.75	1.1	0.097
P234	39	0.15	0.73	18	1.6

SI.7 Shear rheology of P234 WLMs

Creep measurements, taken with a constant stress σ = 0.2 Pa, used to calculate zero-shear viscosities for P234 at 37 °C and 39 °C are shown below. The slope of the creep curve was used to extract a shear rate, which was used to calculate the zero-shear viscosity via $\eta_0 = \sigma/\dot{\gamma}$.
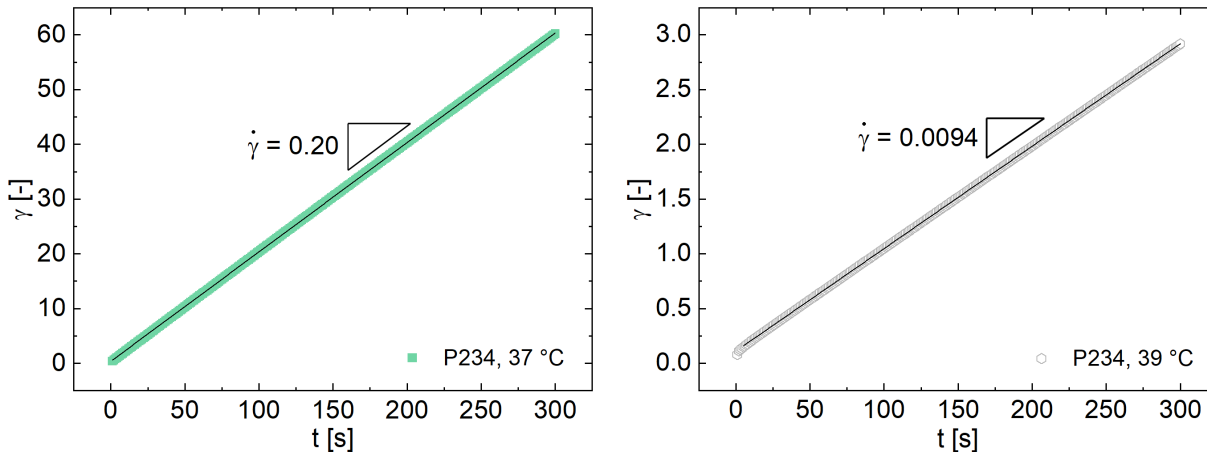

Figure S11: Representative creep measurements for P234 at (a) 37 °C and (b) 39 °C.

The low-shear viscosity of P234 was also measured using a protocol described in the main text. While the linear-linear representation is presented in the main text, the semi-log representation is plotted in Figure S12 below.
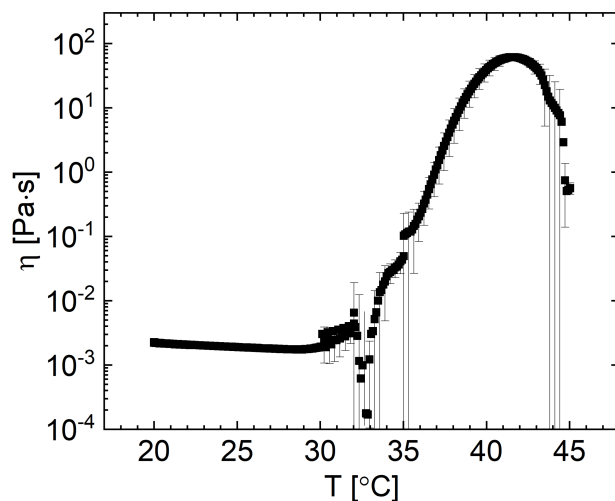
Figure S12: Low shear viscosity η for P234 in 0.9 M NaF on a semi-log plot.

SI.8 Contour length estimations

Cole-Cole plots of P234 WLMs at 37 °C and 39 °C are shown in Figure S13. A semi-circular shape in the Cole-Cole representation is indicative of Maxwellian, fast-breaking behavior in WLMs. The Cole-Cole plot for WLMs at 37 °C (Figure S13a) is not semi-circular, whereas that for WLMs at 39 °C (Figure S13b) is semi-circular.
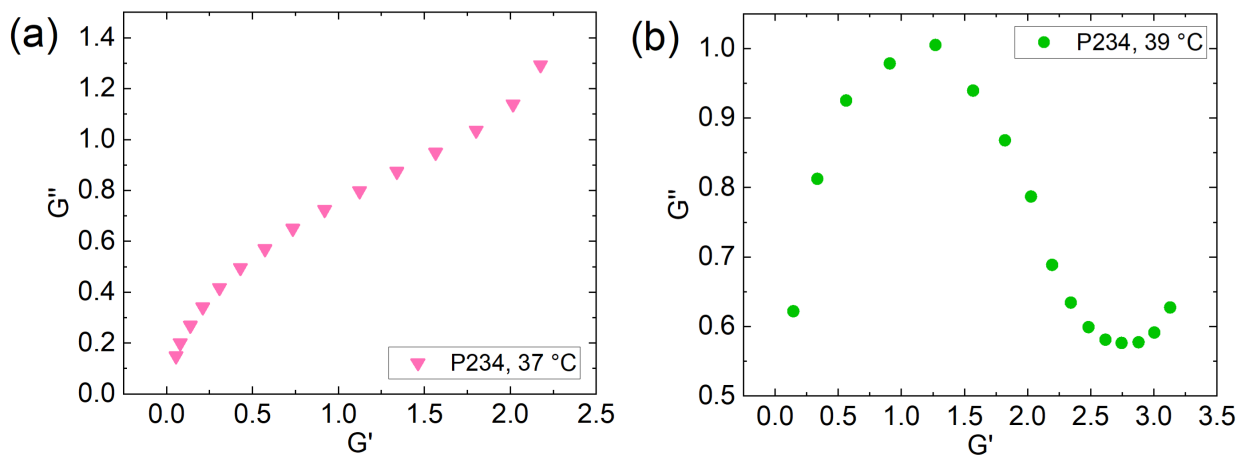

Figure S13: Cole-Cole plots of P234 WLMs at (a) 37 °C and (b) 39 °C. A semi-circular shape like that in (b) is characteristic of Maxwellian, fast-breaking behavior.

For fast-breaking WLMs ($\tau_b << \tau_r$), contour lengths (L_c) can be roughly estimated using the

following relation introduced by Granek and Cates:[9]

$$L_c/l_e \sim G_0/G''_{min} \qquad \text{(SI.8.1)}$$

where G_0 is the plateau modulus, and G''_{min} is the corresponding minimum in loss modulus. The entanglement length l_e can be calculated from using the correlation length ξ:

$$l_e \approx \xi^{5/3}/l_p^{2/3}$$

$$\xi \approx (k_b T/G'_0)^{1/3} \qquad \text{(SI.8.2)}$$

Crude estimates of L_c are tabulated in Table S6. An approximate value of l_p = 64 nm from P234 in NaCl[10] was used for both temperatures. Note that the WLMs at 37 °C do not exhibit a true plateau modulus or minimum in G'' (Figure S11). Thus, for comparison purposes, G_0 and G''_{min} values around the inflection point in G'' at ω = 10 rad/s were chosen to calculate L_c at this temperature for comparison. We note, however, that the result is likely an overestimate.

Table S6: Estimated contour lengths of P234 WLMs at 37 °C and 39 °C. Note that the ratio of G_0/G''_{min} gives an approximate entanglement density.

	T [°C]	G_0/G''_{min}	ξ [μm]	l_e [μm]	L_c [μm]
P234	37	1.7 ± 0.4	0.14 ± 0.01	0.24 ± 0.04	0.4 ± 0.03
P234	39	5.0 ± 1.1	0.12 ± 0.01	0.17 ± 0.01	0.84 ± 0.1

Table S7 below contains l_p values used to estimate L_c for other surfactant WLM systems in the main text. Note l_p for OTAB/NaOA WLMs were unable to be found in the literature, precluding L_c calculations for the system in the main text.

SI.9 Comparing extensional elastic and shear moduli

After fitting radial decay curves to the EC model (Eq. 5), the extensional elastic modulus G_E can be extracted from the exponential prefactor $\left(\frac{G_E R_0}{2\sigma}\right)^{1/3}$. As such, values of G_E determined for 37

Table S7: l_p values used for L_c estimations for surfactant WLMs in the main text.

System	l_p [nm]	Ref.
CPyCl/NaSal 100 mM NaCl brine	20	11
EHAC/NH$_4$Cl	30	12
CPyCl/NaSal	26.7 - 29.8	13
CTAB/NaSal	24[a]	14

[a]average of l_p values at different compositions

°C and 39 °C along with the shear rheology plateau moduli, G_0, determined in SI.8 are shown in Table S8. Unsurprisingly, G_E and G_0 are not in good agreement for P234 at 37 °C; as discussed previously, the LVE shear rheology at this temperature lacks a true plateau modulus, and the radial decay curves exhibit the highest degree of variability due the sharp increase in shear viscosity in this transition region. Conversely, G_E and G_0 are in good agreement for P234 at 39 °C.

Table S8: Extracted extensional elastic moduli and plateau moduli for P234 WLMs.

T [°C]	G_0 [Pa]	G_E [Pa]
37	1.6 ± 0.3	26 ± 6
39	2.8 ± 0.4	2.3 ± 0.5

SI.10 Beads-on-a-string instability

SI.10.1 Multivariate analysis of parameters affecting BOAS formation

To better understand parameters that affect the formation and evolution of BOAS in P234 at 39 °C, a multivariate analysis was conducted on experimental variables such as aspect ratio (AR) and filament length and resulting extensional flow variables such as number of beads and extensional relaxation time. As predicted, the aspect ratio and filament length are strongly correlated with the number of beads that form on the filament, as shown in orange in Figures S14 and S15; longer filaments can sustain more instability wavelengths. Interestingly, the number of beads on a filament do not affect extensional parameters such as duration of thinning Regions I-III or associated extensional relaxation times (green outline, Figures S14 and S15).

	AR	initial # beads	final # beads	initial filament length [mm]	length, RI	length, RII	length, RIII	lambdaE,I	lambdaE,III
AR	1.0000	0.8868	0.7791	0.9645	0.2313	0.0182	-0.3899	-0.0512	-0.6694
initial # beads	0.8868	1.0000	0.9015	0.8945	-0.1708	-0.2594	-0.7371	-0.4133	-0.8563
final # beads	0.7791	0.9015	1.0000	0.8618	-0.2792	-0.1254	-0.4770	-0.4034	-0.4126
initial filament length [mm]	0.9645	0.8945	0.8618	1.0000	0.1472	-0.0700	-0.3925	-0.3245	-0.5664
length, RI	0.2313	-0.1708	-0.2792	0.1472	1.0000	0.6179	0.4190	0.8926	0.7188
length, RII	0.0182	-0.2594	-0.1254	-0.0700	0.6179	1.0000	0.7599	0.8297	0.6137
length, RIII	-0.3899	-0.7371	-0.4770	-0.3925	0.4190	0.7599	1.0000	0.7516	0.8167
lambdaE,I	-0.0512	-0.4133	-0.4034	-0.3245	0.8926	0.8297	0.7516	1.0000	0.4724
lambdaE,III	-0.6694	-0.8563	-0.4126	-0.5664	0.7188	0.6137	0.8167	0.4724	1.0000

Figure S14: Correlations between variables in P234 at 39 °C trials exhibiting BOAS instabilities. Notable correlations showing impact of filament length on number of beads are outlined in orange, and correlations showing how trial-dependent parameters such as AR do not affect extensional parameters are highlighted in green.

None of the rheologically-relevant timescales ($\lambda_{E,I}$, $\lambda_{E,III}$, lengths of region I and III) are correlated with aspect ratio or filament length, which is promising given that prior CaBER studies have shown aspect ratio-dependent rheology.[15,16] We suspect this evidence suggests that small differences in substrate spreading do not play a substantial role in altering the rheological parameters, a topic previously investigated by Wu and Mohammadigoushki[17]. Wu and Mohammadigoushki[17] found that spreading does not impact extracted rheological parameters for low capillary numbers, Ca and spreading velocities but does for higher Ca. Within our operating range, the primary impact of spreading is likely that the spreading velocity and spreading profile alters the 'stability region' of the fluid column, i.e. the overall liquid bridge volume and ultimately the 'effective'

aspect ratio of the fluid.[18] For example, when the droplet is pinned, the lower bulb has a substantially higher height, creating an 'effective' aspect ratio that is substantially smaller than the actual aspect ratio, or the 'effective' aspect ratio achieved in a sample that spreads. If the spreading substantially impacted thinning, the rheological timescales ($\lambda_{E,I}$, $\lambda_{E,III}$, lengths of region I and III) would be expected to be correlated with aspect ratio and thus filament length; however only the bead parameters are correlated with these two geometric variables.
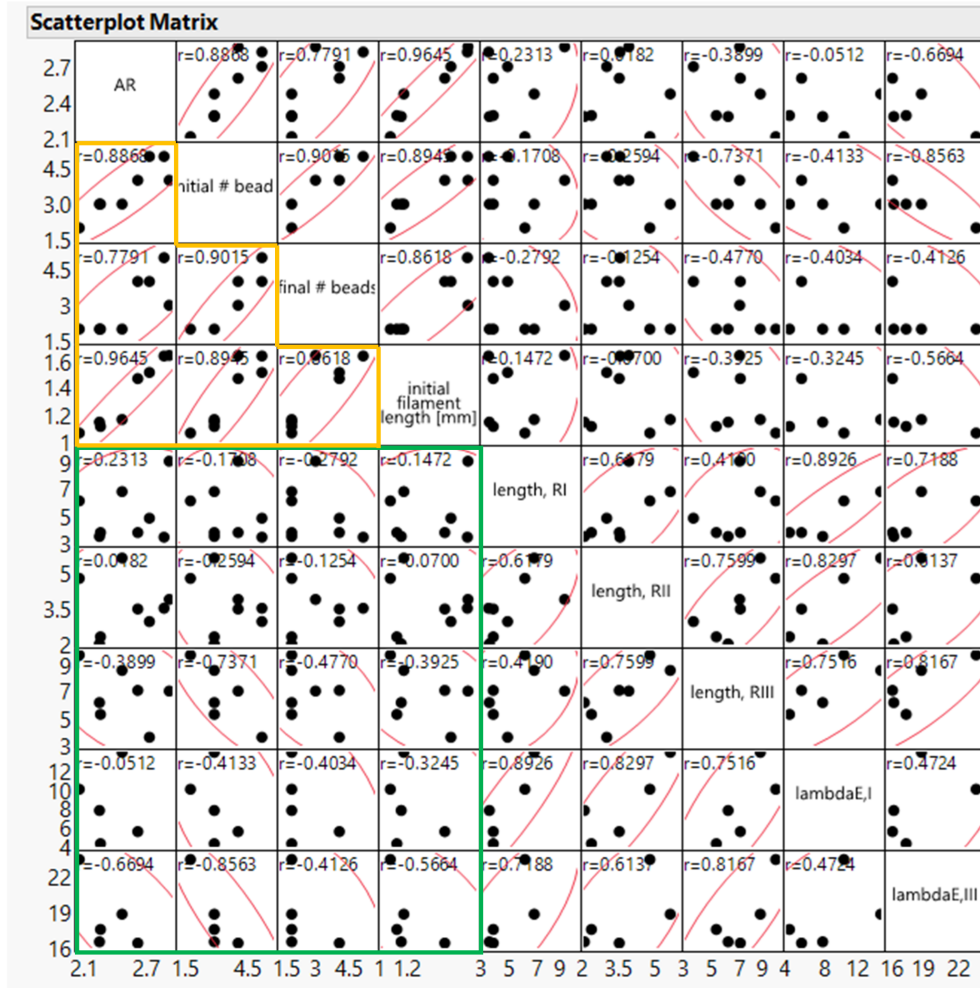

Figure S15: Scatterplot matrix of correlations between variables in P234 at 39 °C trials exhibiting BOAS instabilities. Notable correlations showing impact of filament length on number of beads are outlined in orange, and correlations showing how trial-dependent parameters such as AR do not affect extensional parameters are highlighted in green. Density ellipses are shown to guide the eye.

SI.10.2 Additional analysis of bead formation (region II)

The bead sizes in region II are approximately equal across the filament for even bead numbers ($N = 2, 4$), as shown in Figure 6a (rows i,iv frame 5). However, in both cases starting with three beads (row ii and iii), the beads have drastically different volumes by the end of region II. For the $N = 3$ case (Figure 6a, row iii), the middle bead is larger in volume, which is immediately apparent upon initial bead formation (frame 3); the high-speed images suggest that the larger middle bead may have resulted from early coalescence of two beads during bead formation (frames 2-3). The effect of bead coalescence on bead size is clear in the case where three fully-formed beads coalesce into two beads in region II (Figure 6a, row ii). The three bead sizes are initially similar, but the coalescence of the center and upper bead yields an new bead that is ~25% larger in diameter than the bottom bead in the final frame of region II (Figure S16a).

For beads of equal size ($N = 2, 4$ in Figure 6a), BOAS instabilities arise more symmetrically than when bead sizes are unequal. For example, the terminal beads are found at a nearly identical distance from the top and bottom bulbs at the end of region II for $N = 2, 4$; for $N = 4$, each middle bead is also equidistant from the adjacent terminal bead (Figure 6a, row iv). For the $N = 2$ case, the inter-bead distance is shorter than the distance between each bead and the nearest filament end (Figure 6a, row i). Similarly, for $N = 4$, the distance between the terminal beads and the filament end is greater than the distance between terminal and middle beads; the distance between the two middle beads is the smallest. In these cases, BOAS formation exhibits symmetry about the horizontal midplane as the instability grows from the filament ends towards the middle of the filament. However, for unequal-sized beads (row ii, iii in Figure 6a), beads are located at unequal distances from the filament ends. For example, in the bead coalescence case (Figure 6a, row ii), the top of the larger bead is found ~25% of the way down from the top of the filament, whereas the smaller bead is half as far from the bottom of the filament. Here, the inter-bead spacing falls between these two length scales. For $N = 3$, the upper bead falls near the upper bulb and is fairly close to the middle bead, whereas the bottom bead falls much farther below the middle bead and is also substantially further from the filament end.

SI.10.3   Bead velocities and sizes

Figures S16 and S17 show displacement profiles (column i) and bead sizes (column ii) for region III of all P234 39 °C trials that exhibit the BOAS instability. The spatial location of the curve corresponds with the spatial location of the bead, i.e. the top pink curve corresponds to the top bead on the filament. In many trials, the top bulb coalesces with the upper bulb prior to breakup. The coalescence phenomenon is reflected in the discontinuities seen in Figures S16c-d and S17a-b at the time indicated by the vertical black dashed line. The bead trajectories after the dashed line also indicate how the filament breaks up. For example, in Figure S16, the curves corresponding to the middle and bottom bead shift up after the vertical dashed line, corresponding to coalescence of the top bead. The second bead then moves up while the bottom bead moves down, and the filament breaks in between the second and bottom bead as indicated by the black star.

Table S9: Bead velocities for each P234 39 °C trial shown in Figures S16 and S17. v_1 corresponds to the fits shown in black dashed lines while v_2 corresponds to the fits shown as solid green lines. Positive v values correspond to a bead moving towards the top bulb (up).

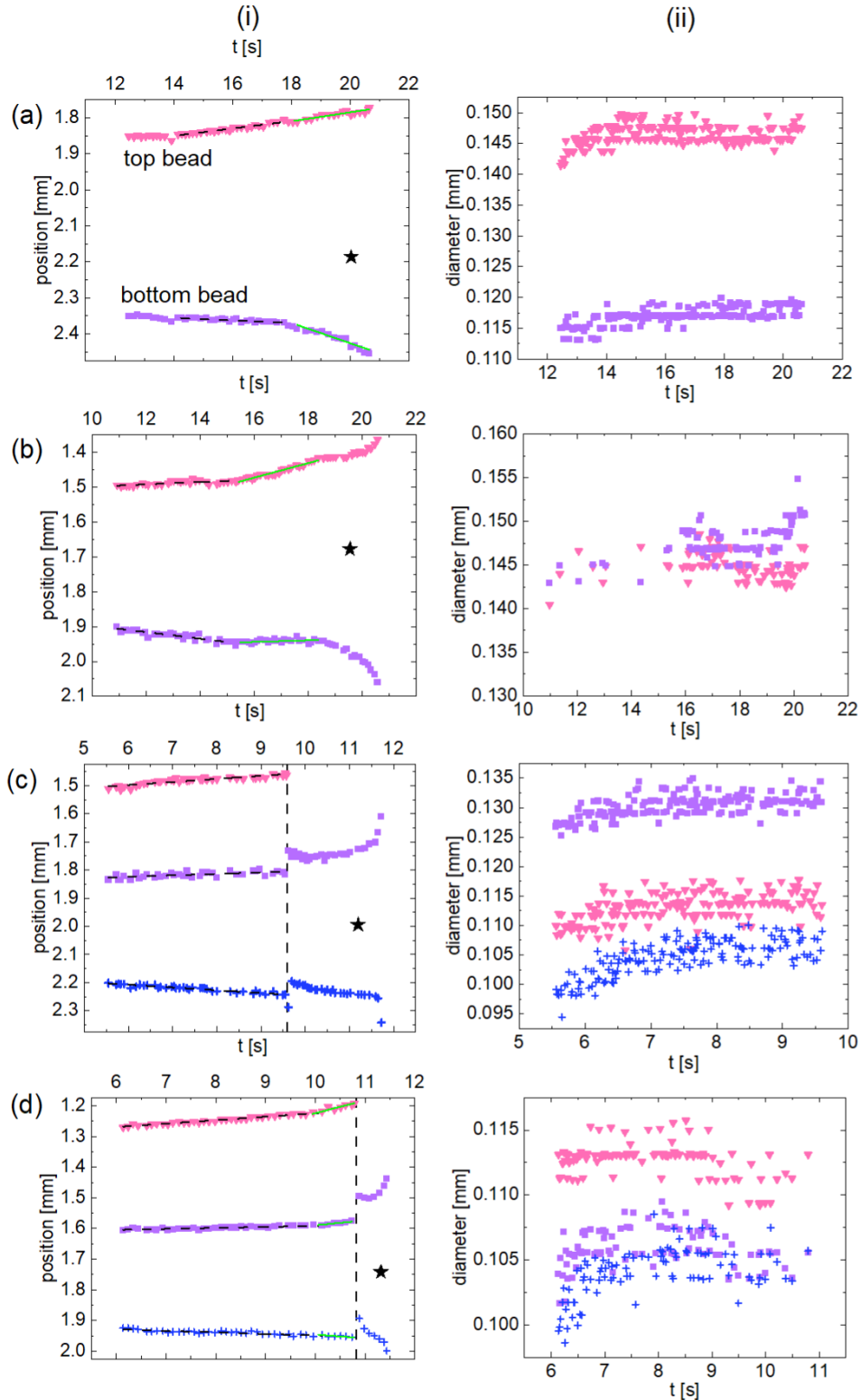|	$v_1 \times 10^2$ [mm/s]					$v_2 \times 10^2$ [mm/s]				
trial	b1	b2	b3	b4	b5	b1	b2	b3	b4	b5
S16a	1.0	-0.36	-	-	-	1.3	-2.8	-	-	-
S16b	0.34	-0.95	-	-	-	2.1	-1.2	-	-	-
S16c	1.1	0.52	-0.98	-	-	-	-	-	-	-
S16d	1.1	0.33	-0.51	-	-	4.2	1.6	0.65	-	-
S17a	2.2	1.6	1.3	0.37	-	3.0	2.0	2.0	-0.67	-
S17b	1.6	0.33	-0.77	-2.5	-	12	5.9	4.9	3.4	-
S17c	1.3	0.73	-0.23	-1.2	-2.3	3.0	2.2	-1.9	-2.7	-3.1

Figure S16: Displacement profiles and bead sizes in Region III for trials that exhibit 2-3 beads. Each row (a-d) corresponds to a distinct trial. Displacement profiles are shown in column (i), and corresponding bead size is shown in column (ii). Vertical dotted black lines indicate discontinuities that result from the top bead coalescing into the top bulb, and the black star symbol indicates the region in which filament breakup occurs.
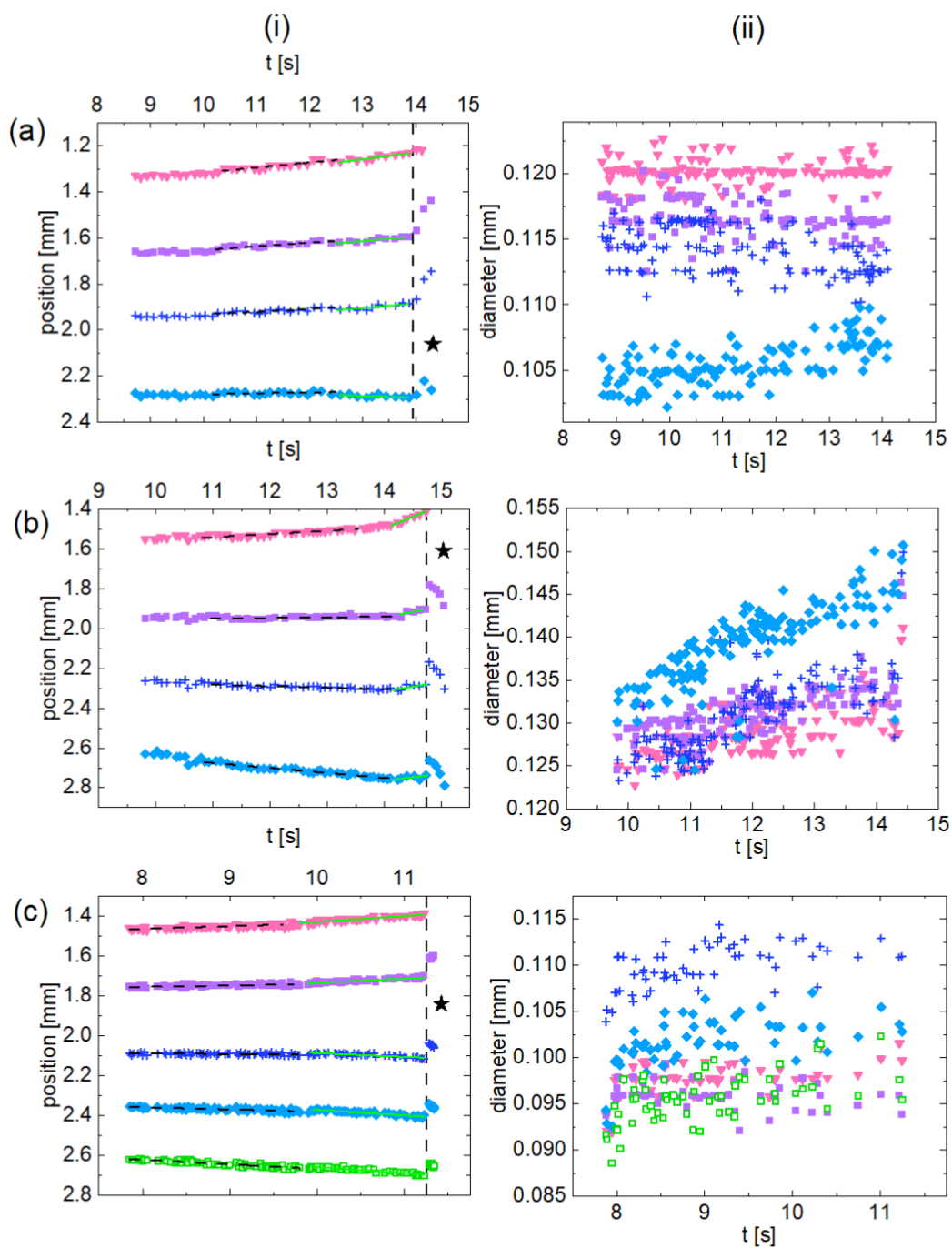
Figure S17: Displacement profiles and bead sizes in Region III for trials that exhibit 4-5 beads. Each row (a-d) corresponds to a distinct trial. Displacement profiles are shown in column (i), and corresponding bead size is shown in column (ii). Vertical dotted black lines indicate discontinuities that result from the top bead coalescing into the top bulb, and the black star symbol indicates the region in which filament breakup occurs.

SI.10.4 Dimensionless parameters for BOAS formation

In their simulations, Chang *et al.* [19] presented four criteria that must be met for BOAS formation to occur based on the Weissenberg number Wi (note that Oliveira and McKinley [20] use the Deborah number $De = \lambda_E / \sqrt{\rho R_0^2 / \sigma}$), the viscosity ratio $S = \eta_s / \eta_0$, the Ohnesorge number $Oh = \eta_0 / \sqrt{\rho \sigma R_0}$, and the finite extensibility parameter L^2, which was estimated from the infinite Trouton ratio Tr^∞ using the theoretical limit for dilute solutions of FENE dumbbells: [20–22] $Tr^\infty \to 2(1-S)L^2$. Table S10 tabulates the parameters used to compare the values between P234 WLMs at 39 °C and PEO solutions studied by Oliveira and McKinley [20]. Calculations using the initial filament radius R_0 and the filament radius near the onset of EC thinning r_{EC} are shown. Using r_{EC} yields a $R/R_0 \sim 0.25$, which was near the onset of EC thinning in PEO solutions studied by Oliveira and McKinley [20], but conclusions do not change. Figure S18 shows the slender filament shape at $R/R_0 \sim 0.25$, confirming the proximity to EC thinning.

Table S10: Parameters related to iterated stretching calculated using the initial filament radius R_0 and R_{EC} for P234 WLMs and PEO solutions. [20]

	R_0 [mm]	R_{EC} [mm]	σ [mN/m]	η_0 [Pa·s]	λ_E [s]	Oh	S	De	L^2	Wi	Ca	Ec
P234	0.64	-	29	25	8.4	176	$3.2 \cdot 10^{-5}$	$2.7 \cdot 10^3$	$1.4 \cdot 10^2$	$4.7 \cdot 10^5$	$3.1 \cdot 10^4$	$1.5 \cdot 10^1$
P234	-	0.16	29	25	8.4	351	$3.2 \cdot 10^{-5}$	$2.2 \cdot 10^4$	$1.4 \cdot 10^2$	$7.6 \cdot 10^6$	$1.2 \cdot 10^5$	$6.1 \cdot 10^1$
PEO	0.6	-	62	$4.7 \cdot 10^{-2}$	0.23	0.25	$1.4 \cdot 10^{-1}$	$1.3 \cdot 10^2$	$8.4 \cdot 10^4$	$3.2 \cdot 10^1$	$6.4 \cdot 10^{-2}$	$5.1 \cdot 10^2$

Figure S18: Representative image frame at $R/R_0 \sim 0.25$, showing nearly slender filament shape near onset of EC thinning in P234 at 39 °C.

SI.10.5   BOAS vs. blistering instabilities

Previous filament thinning studies of dilute PEO solutions also suggested that multiple generations of beads formed in time,[2023] where beads within each generation were of similar size. In PEO solutions, one generation of large beads formed initially; then, as the filaments between beads pinched, subsequent satellite beads of a smaller size formed in between the first generation of beads. Up to four generations of beads have been observed in PEO solutions,[2023] with bead size decreasing with each successive generation prior to breakup. These blistering instabilities occur during late stages of filament thinning and have been attributed to partial relaxation of highly extended chains and phase separation between polymer and solvent,[23–26] though a range of other mechanisms have also been proposed.[19202227] Notably, these blistering instabilities occur immediately prior to breakup, where the radius decays more rapidly[202328] and assumes a linear rather than exponential decay profile.[232528]

While P234 WLMs appear to primarily exhibit only one generation of beads, evidence of secondary beads can be seen in region III when $N \geq 3$ (Figure 6b.iii-iv). For both of these cases, two small second-generation beads appear to form – one between the bottom bulb and the terminal bead and another between the lower two beads. However, even though secondary beads are observed in some P234 trials, the presence of blistering instabilities similar to those observed in PEO solutions is unlikely. In contrast to PEO solutions, the linear radial decay region immediately prior to breakup where blistering instabilities are well-documented[202328] is not observed in any P234 trial (within the camera resolution); rather than transitioning to a linear radial decay profile, the P234 filament ruptures rapidly at the end of region III. Additionally, at the onset of the blistering instability in polymer solutions,[2326] the beads across all generations are highly spherical whereas this spherical shape is never observed in P234 WLMs. However, small secondary beads resembling those seen in the P234 WLMs have been observed in dilute PEO at the end of the BOAS instability region, immediately prior to the onset of blistering instabilities[2028]; these similarities suggest the secondary beads in P234 WLMs correspond to BOAS instabilities rather than blistering instabilities. Given that the P234 filament ruptures rapidly at the end of region III, short-lived

blistering instabilities could still occur; alternatively, filament rupture due to WLM breakage[2930] could also explain this behavior. Finally, as high viscosity dampens BOAS progression,[3132] the much higher solution viscosity of the P234 WLMs could also mitigate phase separation-induced blistering instabilities[2526] by reducing WLM mobility in solution.

SI.11   Analysis of CaBER vs. DoS data

Linear regression analysis was performed on the five linear, fast breaking WLMs measured by Omidvar *et al.*[33] using CaBER and DoS (Table S11), using an equation of the form $y = mx + b$ where y is Tr_{max} and $x = \lambda_E/\lambda_s$, the ratio of extensional and shear relaxation times. The 95% confidence interval around the slope m and intercept b are reported for each method. The y-intercept fit is not statistically significant for either CaBER or DoS, as the 95% confidence interval encompasses zero. For CaBER measurements, the 95% confidence interval also encloses zero, meaning that there is no statistically significant change in Tr_{max} with increasing relaxation time ratio. However, Tr_{max} is positively, linearly correlated with the relaxation time ratio for DoS measurements ($R^2 = 0.98$); the much narrower 95% confidence interval does not enclose zero.

Table S11: Regression analysis parameters for CaBER vs. DoS data from Omidvar *et al.*[33]; m is the slope and b is the y-intercept. As discussed in the main text, the 95% confidence intervals around both regression parameters for CaBER trials enclose zero, meaning neither is statistically significant. The slope is statistically significant at the 95% confidence level for DoS measurements, indicating that Tr_{max} increases with λ_E/λ_s for DoS measurements.

method	N	m	95% CI	b	95% CI	R^2
DoS	5	372	265 – 478	2.3	-34.1 – 38.7	0.98
CaBER	5	189	-1 – 378	-3.1	-50.9 – 44.7	0.77

If instead the CTAB/NaSal WLMs examined by Bhardwaj *et al.* [29] using CaBER are included, a similar trend in the DoS vs. CaBER data is observed though a slightly higher Tr_{max} is observed ($Tr_{max} \approx 200$, Figure S19). The CaBER data remains randomly distributed with λ_E/λ_s with this additional data. If this higher Tr_{max} was the limiting value for linear WLMs, the general conclusions about DoS vs. CaBER are still applicable, as Tr_{max} for DoS still exceeds CaBER values significantly with increasing λ_E/λ_s. However, these CTAB/NaSal WLMs are thought to be branched, as prior work by Sachsenheimer *et al.* [34] showed that these salt-to-surfactant molar ratios, [R], occur after the first maximum in the zero-shear viscosity with increasing [R] – a clear signature of WLM branching. Note that the branched WLMs examined by Omidvar *et al.* [33] using DoS also follow a linear relationship with λ_E/λ_s; here $m = 626$, which falls above the data for linear micelles using DoS ($m = 372$, Table S11). Additional data by Calabrese and Wagner [35] also show higher Tr_{max} for branched vs. linear WLMs. Accordingly, the higher Tr_{max} when the 'branched' CTAB/NaSal WLMs are included in Figure S19 likely reflects the branched microstructure (and ability of these WLMs to relieve stress by sliding branch points), rather than true change in the Tr_{max} limit for linear WLMs. Note that the trends in DoS data persist despite differences in instrument and instrument configuration. Data by Wu and Mohammadigoushki [17] and Omidvar *et al.* [33] were taken on the same instrument but with different substrate spreading; data for P234 WLMs was taken on a different DoS device than the prior two studies.
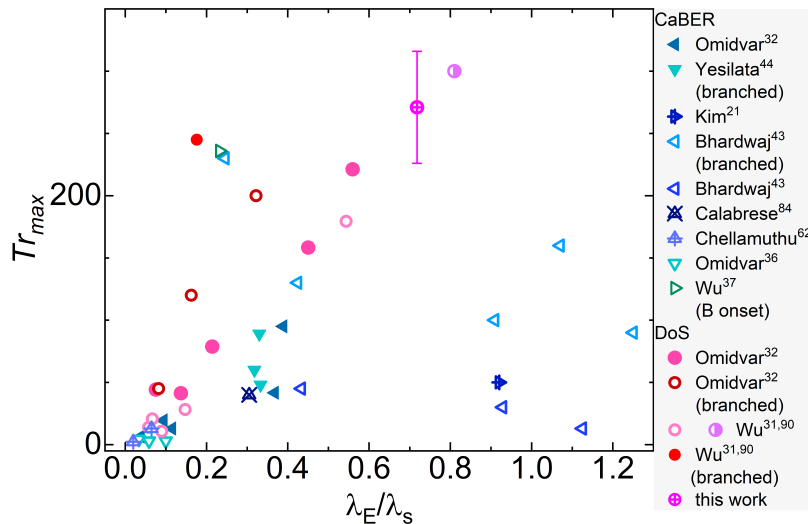
Figure S19: Tr_{max} for fast-breaking WLMs as a function of relaxation time ratio, λ_E/λ_s, measured in CaBER (blue $\triangle$) vs. DoS (pink $\bullet$); ref. numbers refer to the main text. WLMs measured via DoS show a clear increase in Tr_{max} with increasing λ_E/λ_s; corresponding CaBER trials appear randomly distributed, likely due to breakage during the initial step strain. CaBER trials coded by sample and reference show that even within the same system or operating parameters, no trend in Tr_{max} with increasing λ_E/λ_s is observed. Additional CaBER data from micelles thought to be branched is included, along with DoS trials on branched WLMs. Branched WLMs appear to achieve larger Tr_{max} than linear WLMs.

References

[1] J. Dinic and V. Sharma, *Proc. Natl. Acad. Sci.*, 2019, **116**, 8766–8774.

[2] G. H. McKinley, *Rheol. Rev.*, 2005, 1–48.

[3] M. A. Fontelos and J. Li, *J. Non-Newton. Fluid Mech.*, 2004, **118**, 1–16.

[4] J. Dinic, Y. Zhang, L. N. Jimenez and V. Sharma, *ACS Macro Lett.*, 2015, **4**, 804–808.

[5] A. Deblais, M. Herrada, I. Hauner, K. Velikov, T. van Roon, H. Kellay, J. Eggers and D. Bonn, *Phys. Rev. Lett.*, 2018, **121**, 254501.

[6] K. T. Lauser, A. L. Rueter and M. A. Calabrese, *Soft Matter*, 2021, **17**, 9624–9635.

[7] C. Clasen, *Korea Aust. Rheol. J.*, 2010, **22**, 9.

[8] S. L. Anna and G. H. McKinley, *J. Rheol.*, 2000, **45**, 115–138.

[9] R. Granek and M. E. Cates, *J. Chem. Phys*, 1992, **96**, 4758.

[10] M. Duval, G. Waton and F. Schosseler, *Langmuir*, 2005, **21**, 4904–4911.

[11] D. Gaudino, R. Pasquino and N. Grizzuti, *J. Rheol.*, 2015, **59**, 1363–1375.

[12] J. T. Padding, W. J. Briels, M. R. Stukan and E. S. Boek, *Soft Matter*, 2009, **5**, 4367.

[13] C. Oelschlaeger, M. Schopferer, F. Scheffold and N. Willenbacher, *Langmuir*, 2009, **25**, 716–723.

[14] F. Nettesheim and N. J. Wagner, *Langmuir*, 2007, **23**, 5267–5269.

[15] N. J. Kim, C. J. Pipe, K. H. Ahn, S. J. Lee and G. H. McKinley, *Korea Aust. Rheol. J.*, 2010, **22**, 11.

[16] E. Miller, C. Clasen and J. P. Rothstein, *Rheol. Acta.*, 2009, **48**, 625–639.

[17] S. Wu and H. Mohammadigoushki, *Phys. Rev. Fluids*, 2020, **5**, 053303.

[18] L. A. Slobozhanin and J. M. Perales, *Phys. Fluids*, 1993, **5**, 1305–1314.

[19] H.-C. Chang, E. A. Demekhin and E. Kalaidin, *Phys. Fluids*, 1999, **11**, 1717–1737.

[20] M. S. N. Oliveira and G. H. McKinley, *Phys. Fluids*, 2005, **17**, 071704.

[21] A. Lindner, J. Vermant and D. Bonn, *Phys. A: Stat. Mech. Appl.*, 2003, **319**, 125–133.

[22] J. Li and M. A. Fontelos, *Phys. Fluids*, 2003, **15**, 922–937.

[23] R. Sattler, S. Gier, J. Eggers and C. Wagner, *Phys. Fluids*, 2012, **24**, 023101.

[24] H. V. M. Kibbelaar, A. Deblais, F. Burla, G. H. Koenderink, K. P. Velikov and D. Bonn, *Phys. Rev. Fluids*, 2020, **5**, 092001.

[25] J. Eggers, *Phys. Fluids*, 2014, **26**, 033106.

[26] A. Deblais, K. Velikov and D. Bonn, *Phys. Rev. Lett.*, 2018, **120**, 194501.

[27] M. S. N. Oliveira, R. Yeh and G. H. McKinley, *J. Non-Newton. Fluid Mech.*, 2006, **137**, 137–148.

[28] R. Sattler, C. Wagner and J. Eggers, *Phys. Rev. Lett.*, 2008, **100**, 164502.

[29] A. Bhardwaj, E. Miller and J. P. Rothstein, *J. Rheol.*, 2007, **51**, 693–719.

[30] J. P. Rothstein, *J. Rheol.*, 2003, **47**, 1227–1247.

[31] A. M. Ardekani, V. Sharma and G. H. McKinley, *J. Fluid Mech.*, 2010, **665**, 46–56.

[32] P. P. Bhat, S. Appathurai, M. T. Harris, M. Pasquali, G. H. McKinley and O. A. Basaran, *Nat. Phys.*, 2010, **6**, 625–631.

[33] R. Omidvar, S. Wu and H. Mohammadigoushki, *J. Rheol.*, 2019, **63**, 33–44.

[34] D. Sachsenheimer, C. Oelschlaeger, S. Müller, J. Küstner, S. Bindgen and N. Willenbacher, *J. Rheol.*, 2014, **58**, 2017–2042.

[35] M. A. Calabrese, *Developing structure-property relationships in branched wormlike micelles via advanced rheological and neutron scattering techniques*, University of Delaware, 2017.